Visualization of dynamic noise current distribution from Si and SiC power devices based on time-synchronized near magnetic field scanning

Takaaki Ibuchi, Tsuyoshi Funaki
Osaka University
Div. of Electrical, Electronic and Information Eng., Graduate school of Engineering,
Suita, Osaka 565-0871, Japan
Email: ibuchi@eei.eng.osaka-u.ac.jp

***Abstract*— This report studies the visualization of dynamic noise current distribution in switching operation of Si and SiC power devices. The measurement system is developed to identify time-dependent near magnetic field distribution for periodic steady state circuit operation. The experimental results shown in this report demonstrate the usefulness of the developed system to identify the EMI noise generation and to visualize the time variation of noise current distribution in the power conversion circuit.**

Keywords—; near magnetic field intensity; dynamic noise current behavior; visualization technology; Si IGBT; SiC MOSFET

I. INTRODUCTION

The power conversion circuits require to be operated at higher switching frequency with the increasing demand for high-power density. The emerging SiC MOSFETs are an attractive replacement of Si IGBTs for high power application such as automotive and aerospace [1, 2]. However, the large di/dt and dv/dt leads to an adverse effect of increasing electro-magnetic interference (EMI) [3-6]. It is difficult to measure a high-voltage and a large-current including radio frequency (RF) noise component with high accuracy in a highly-integrated power conversion circuit. Our previous research work focuses the current distribution in a SiC power module identified with magnetic near-field intensity for optimizing layout design [7]. The identification of EMI noise source and the clarification of noise propagation in a power conversion circuit is important to reduce the EMI noise level. This report develops measurement system and visualizes noise current distribution associated with its periodic steady-state switching operation, based on scanned time-synchronized near magnetic field measurement. This report demonstrates the visualization of difference in noise generation and its propagation characteristics between Si and SiC power devices.

II. DEVELOPED MEASUREMENT SYSTEM AND DEVICE UNDER TEST

A. Time-synchronized near magnetic field scanning system

Figure 1 (a) shows the conventional configuration of 2-D near magnetic field scanning system. A magnetic probe is connected to a swept-tuned spectrum analyzer in a measurement system (IEC standard 61967-6, magnetic probe method). The system is controlled via GUI on a PC display. The magnetic probe scans over the near field of the device under test (DUT), and stores the measured data in the PC. The magnetic field intensity is measured in two orthogonal directions (H_x, H_y) at each measurement point, and then magnetic field amplitude H_{xy} is post-calculated. The distribution of frequency spectrum in current density can be visualized based on the scanned H_{xy}. The conventional spectrum analyzer measures broadband frequency range spectrum with peak or quasi-peak detection, however, time variations of the magnetic field are not attainable. The EMI noise source in a switching power converter is the transient voltages and currents variation caused by the switching operations of power semiconductor devices in the circuit. Therefore, visualization of the noise component behavior in time domain is useful to clarify the EMI noise generation mechanisms in power electronics circuits. This report focuses on the dynamic noise current distribution in a power converter along with the switching operation. Fig. 1 (b) shows the developed system configuration of dynamic near magnetic field measurement. The developed system uses a real-time spectrum analyzer. A magnetic field probe is connected to the RF input of the real-time spectrum analyzer. The gate signal of the transistor is used as the synchronous trigger for real-time spectrum analyzer. Time-synchronization of measurement is secured for periodic steady state operation. The PC controls the magnetic probe position and records the acquisition data. The stored data of time-synchronized near field intensity for the respective measurement point are analyzed with the short-time Fourier transform (STFT) in time-frequency mixed domain [8] as a function of the real-time spectrum analyzer. The developed system measures the time evolution of frequency spectrum of near magnetic field along with the triggered switching operation and spacially scans in 2-D. The measured time-synchronized near magnetic field intensity for scanned power

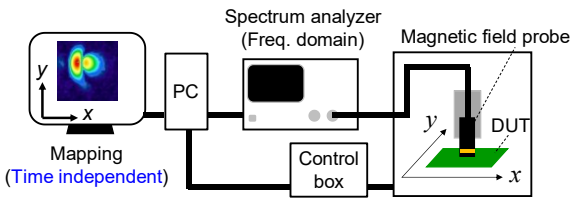

(a) Conventional measurement system

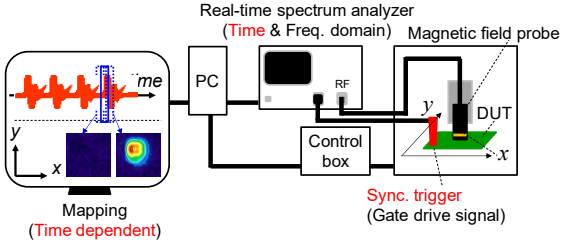

(b) Developed measurement system

Fig. 1. Test setup for evaluating dynamic near magnetic field.

978-1-7281-5579-1/20/$31.00 ©2020 IEEE

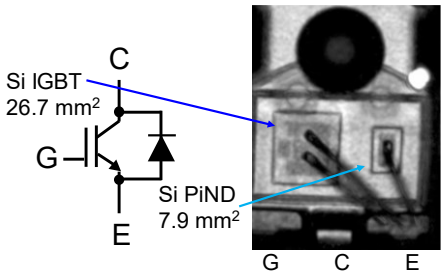

(a) Si IGBT with anti-parallel Si PiN diode

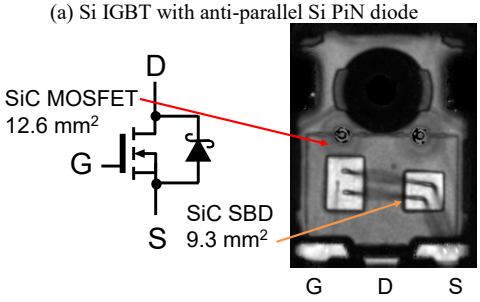

(b) SiC MOSFET with anti-parallel SiC SBD

Fig. 2. Scaning acoustic tomography observation of the studied transistor.

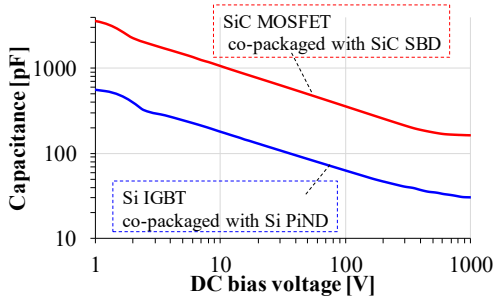

(a) Output capacitance of Si IGBT and SiC MOSFET

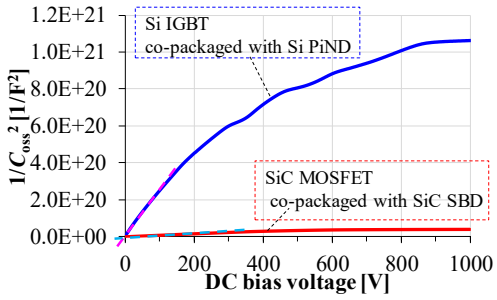

(b) $1/C_{oss}^2$ – V characteristics

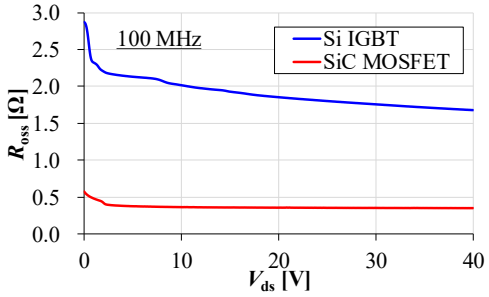

(c) Effective ESR of output capacitance

Fig. 3. C-V charctaeristics of the Si and SiC power devices.

converter is presented as a colored graphic map for the specific time and frequency. A sequence of magnetic field intensity map, shown as a "flip book", visualizes the dynamic characteristics of noise current propagation along with the time. An experimental example of this approach is shown in the following section.

B. Static characteristics of Si and SiC power device

This section shows the static characteristics of the studied Si IGBT (Infineon, IKW25N120H3) and SiC MOSFET (Rohm, SCH2080KE). These devices were co-packaged with anti-parallel diode in a TO-247 package, as depicted in Fig. 2. Fig. 3 (a) shows the DC bias voltage dependency in output capacitance C_{oss}, which is measured by power device analyzer (Keysight, B1505A) with a 100 mV, 1 MHz AC signal for 25 °C. The output capacitance affects the turn-off characteristics. The C_{oss} of SiC MOSFET is larger than that of Si IGBT. This is due to higher impurity concentration in the drift region of the SiC MOSFET than in that of Si IGBT. Fig. 3 (b) shows the $1/C_{oss}^2$ – V characteristics that obtained from the measured C_{oss} – V characteristics shown in Fig. 3 (a) in order to estimate the impurity concentration of the drift layer. The IGBT of bipolar device shows large slope shown in the graph despite of larger die size. This means that the low-impurity concentration of the drift layer in IGBT. Fig. 3 (c) shows the voltage dependency of the effective series resistances (ESR) in the measurement of terminal capacitance in the transistors, which were measured by impedance analyzer (Keysight, E4990A). These are the real part of the drain-source impedance in off-state condition. The Si IGBT has higher ESR than the SiC MOSFET, that is qualitatively coincide with the results of Fig. 3 (b). The drift region in IGBT attains high conductivity by modulating with injected minority carrier. Therefore, the conductance of the drift region in IGBT is lower than in MOSFET.

III. Switching Characteristics of Si and SiC Power Devices

This section discusses the transient behaviors of the Si and SiC power devices in switching operations. The circuit diagram for double-pulse test with clamped inductive load is shown in Fig. 4. The test condition is summarized in Table 1. The co-packed Si PiND of the Si IGBT or the co-packed SiC SBD of the SiC MOSFET in high-side is used as a freewheeling diode. The dynamic behavior of voltage and current of the low-side transistor is evaluated. The evaluation of DUTs was performed for the same design circuit board with different type power device.

TABLE I. Test Condition of Double-Pulse Test

DC input voltage E	300 V
Inductive load L	150 µH
Input capacitor C_{in1}, C_{in2}	20 µF
Snubber capacitor C_{sn1}, C_{sn2}	1 µF // 4 (parallel connected)
1st pulse width Δt	10 µs
Amplitude of conduction current Δi	20 A
Gate drive voltage	+20/0 V (Gate resistor: 1 Ω)

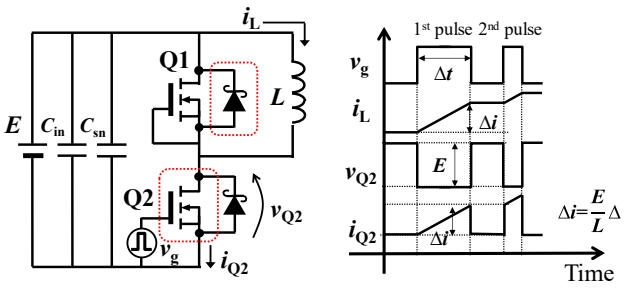

Fig. 4. Double-pulse test.

Fig. 5 shows the transient characteristics in turn-off operation of the low-side transistor. The distinctive differences between Si IGBT and SiC MOSFET are found in voltage and current behavior. The faster switching of SiC MOSFET leads to larger surge voltage and less damped ringing oscillation than that of Si IGBT, regardless of the type of high-side freewheeling diode. They have the same parasitic inductance intrinsic in the same experimental circuit setup. Therefore, the difference in the damping characteristics can be attributed to the effective ESR in the terminal capacitance, as depicted in Fig. 5 (b). Si IGBT does not exhibit high-frequency ringing oscillation in voltage and current in turn-off operation. However, the minority carrier injected into the drift region during the forward conduction results in a tail current. Thus, it leads to a slow turn-off speed and large switching losses of Si IGBT.

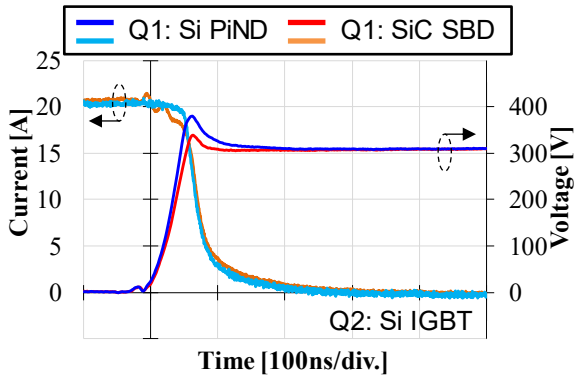

(a) Q2: Si IGBT

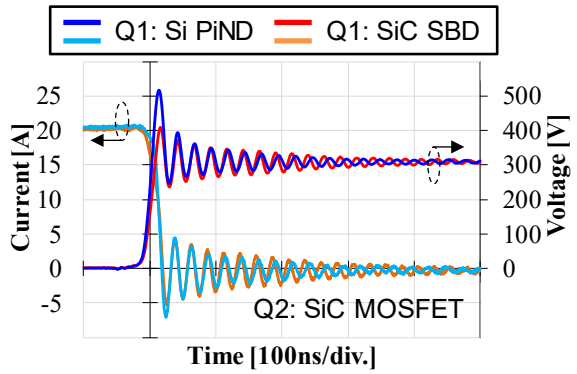

(b) Q2: SiC MOSFET

Fig. 5. Turn-off charctaeristics of Si and SiC power transistors.

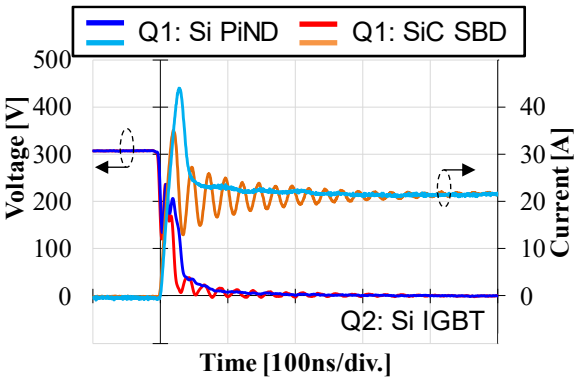

(a) Q2: Si IGBT

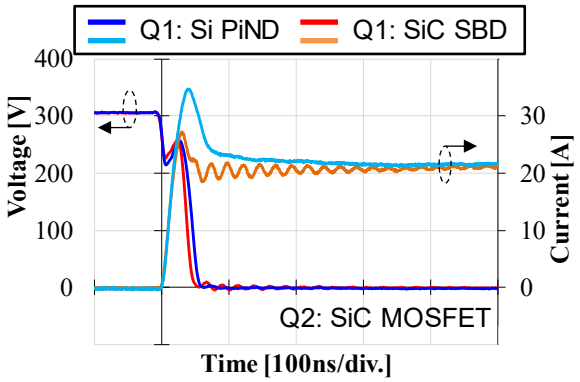

(b) Q2: SiC MOSFET

Fig. 6. Turn-on charctaeristics of Si and SiC power transistors.

The transient voltage and current response in turn-on operation of the low-side transistor is depicted in Fig. 6. The inductive load switching causes commutation from the high-side diode to pass through the low-side transistor. The large reverse recovery current of PiN diode leads to a large current overshoot in the low-side transistor at turn on operation. The tested Si PiN diode shows soft recovery characteristics. SiC SBD causes the hard recovery characteristics and occurs distinct slow-damped ringing oscillation. This is also due to the small ESR in the unipolar device. Thus, the turn-off characteristics of the high-side freewheeling diode dominantly influences on the turn-on behavior of low-side transistor. The turn-on switching speed of the tested Si IGBT is faster than that of SiC MOSFET. Therefore, the amplitude of ringing oscillation in the current of Si IGBT at turn-on operation is larger than for SiC MOSFET. Next section shows an example of visualized dynamic noise current distribution for noise characterization of Si and SiC power devices based on the developed time-synchronized near magnetic field scanning system, explained in section II-A.

IV. Experimental Results of Dynamic Noise Current Visualization

Figure 7 shows the two types double-pulse test circuit diagram for identifying the noise current distribution of Si and SiC power devices. The two phase-leg configurations are parallel-connected for evaluation the dynamic noise current distribution to visualize the difference of noise characteristics

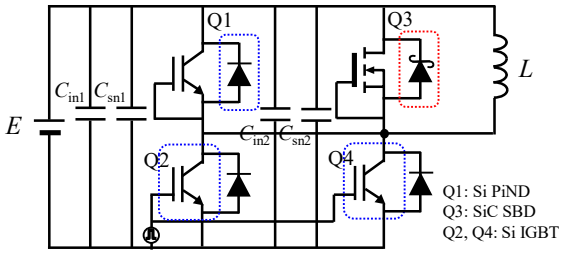

(a) Type A configuration

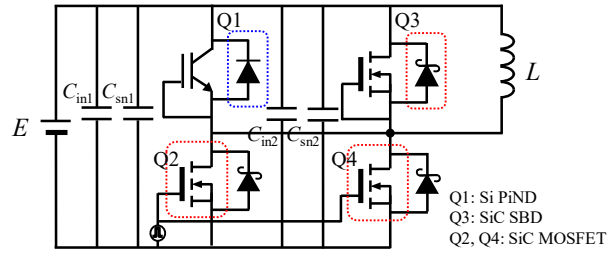

(b) Type B configuration

Fig. 7. Test circuit configuration for time-synchronized near magnetic field scanning.

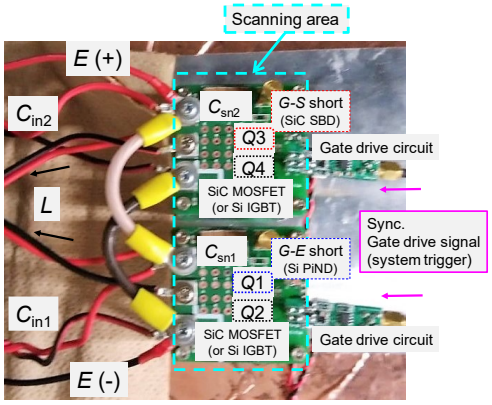

Fig. 8. Scannning area of the circuit under test.

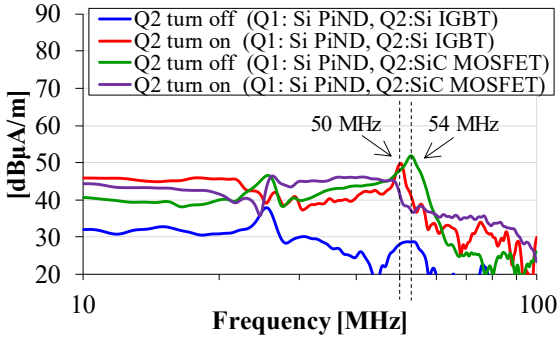

(a) Phase leg: Q1 - Q2

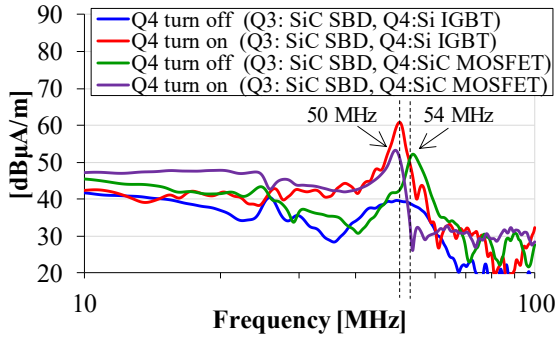

(b) Phase leg: Q3 - Q4

Fig. 9. Frequency spectrum of magnetic field near the test circuit at the switching operation of low-side transistor.

between the Si and SiC power devices simultaneously. The Si IGBTs are used as the low-side transistors Q2 and Q4 in the type A configuration (Fig. 7 (a)). The type B configuration used SiC MOSFETs as Q2 and Q4 transistors (Fig. 7 (b)). The high-side power devices are the same for both configuration; Q1: Si PiND and Q3: SiC SBD. The experimental conditions are same as in the previous section (Table 1). The scanning area of the near magnetic field in the test circuit is demonstrated as Fig. 8. The height of scanning was set to above 50 mm from the surface of PCB. A mixed-domain oscilloscope (Tektronix, MDO4104B-6) was used as the real-time spectrum analyzer in the system shown in Fig. 1 (b). The magnetic field probe (NEC Engineering, MP-10L) was connected to the RF input of the mixed-domain oscilloscope. The gate signal for Q2 and Q4 are used as the synchronous trigger, and the RF signal is simultaneously captured. Then, time-frequency spectrum (spectrogram) of near magnetic field is obtained with synchronizing operation of the low-side transistors.

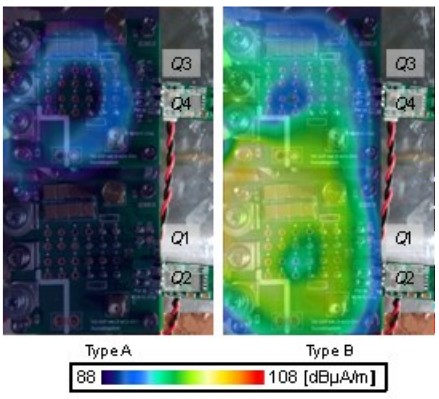

(a) at turn-off operation of low-side transistor

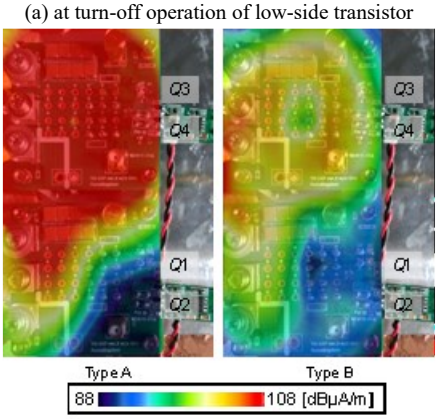

(b) at turn-on operation of low-side transistor

Fig. 10. Noise current distribution in swiching operation (50 MHz).

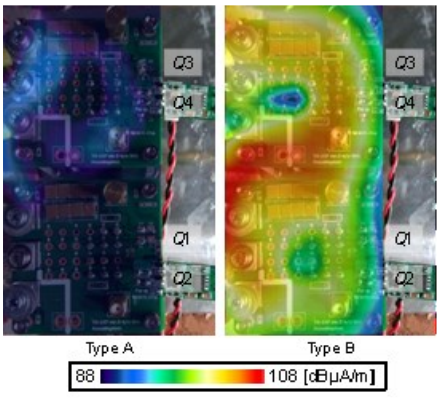

(a) at turn-off operation of low-side transistor

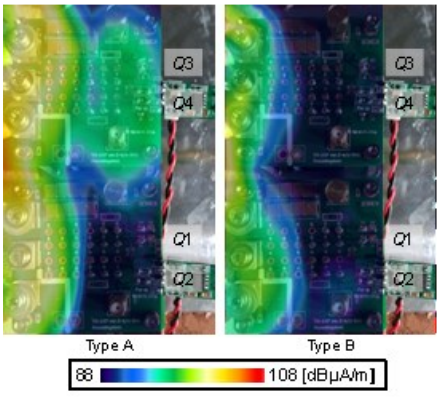

(b) at turn-on operation of low-side transistor

Fig. 11. Noise current distribution in swiching operation (54 MHz).

Fig. 9 shows the frequency spectrum of magnetic field intensity in 10 – 100 MHz near the each phase legs (Q1 – Q2 and Q3 – Q4) synchronized with the switching operations.

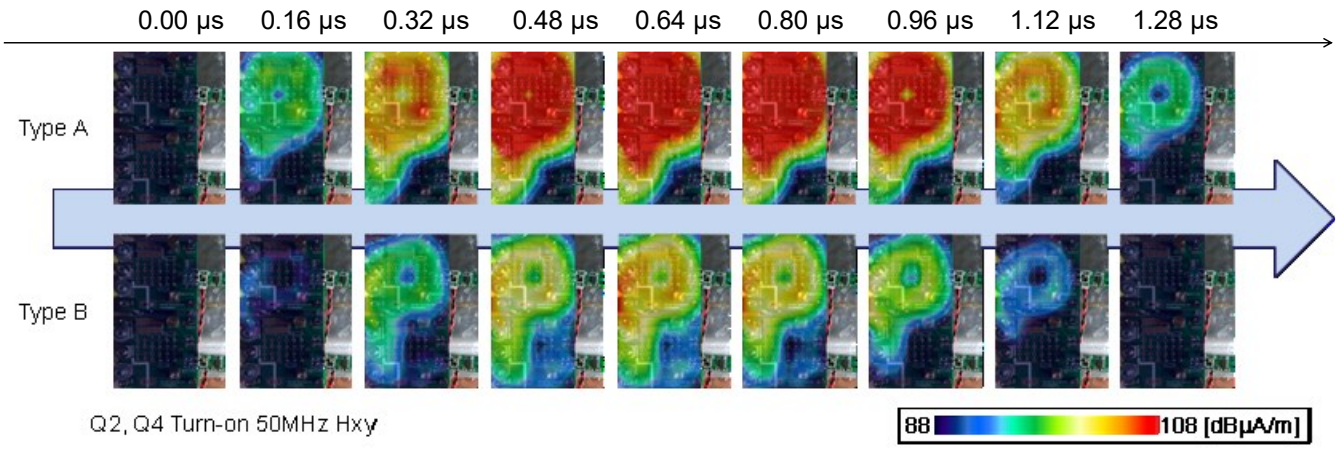

(a) 50 MHz in turn on operation of low-side transistor

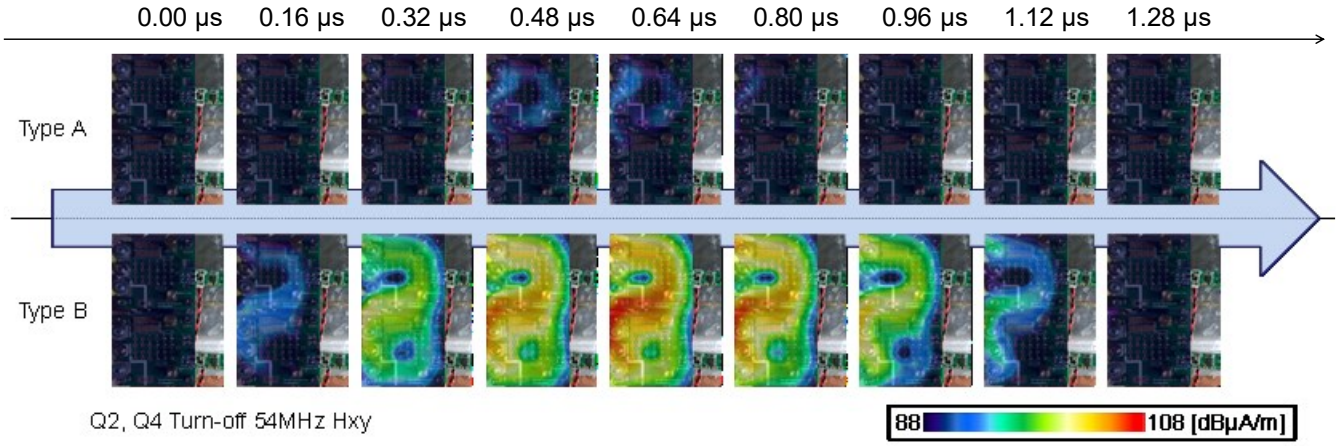

(b) 54 MHz in turn off operation of low-side transistor

Fig. 12. Time variation of noise current intensity distribution in swiching operation based on the developed evaluation system.

These results suggest that the spectrum peak at 50 MHz appears in turn-on operation of the low-side transistor. Its spectrum peak level for using Si IGBT is 4 – 8 dB higher than for using SiC MOSFET. The spectrum peak level at 50 MHz for using SiC SBD is 6 – 10 dB higher than for using Si PiND. The 54 MHz spectrum peak appears especially in turn-off operation of the SiC MOSFET regardless of the freewheeling diode type. The spectrum level of 54 MHz for using Si IGBT as a switching transistor do not show the distinct peak. Based on the results of frequency spectrum characteristics shown in Fig. 9, the near magnetic field distribution of the 50 MHz and 54 MHz components at switching operation were visualized using the proposed measurement system.

Figs. 10 and 11 depict the example of the extracted noise current distribution at turn-on and turn-off operation of Q2 and Q4. The 50 MHz component appears especially in turn-on operation of the low-side transistor, as shown in Fig. 10. The ringing oscillation results from the resonance between the output capacitance of the high-side power device in blocking condition and parasitic inductance in the power loop. The power loop is the current path from the input DC-link capacitor C_{sn} through the half-bridge leg, and back to the C_{sn}. The high 50 MHz noise current intensity at turn on operation exhibits near $Q_3 - Q_4 - C_{sn2}$ power loop, that contains SiC SBD, as depicted in Fig. 10 (b). The 6 dB higher intensity has appeared for the type A configuration than that for the type B, which stems from the fast switching of Si IGBT than SiC MOSFET, as shown in Fig. 6. The extracted 54 MHz noise current component is shown in Fig. 11. The highest level of 54 MHz component is observed in turn-off operation of SiC MOSFET in the type B configuration, as shown in Fig. 11 (a). The ringing oscillation in the current at the turn-off operation of SiC MOSFET exhibits the power loop both $Q_1 - Q_2 - C_{sn1}$ and $Q_3 - Q_4 - C_{sn2}$ loops; that corresponds with the dynamic response of the drain current of the SiC MOSFET at turn-on operation, as shown in Fig. 6. This noise current distribution differs from the results of 50 MHz noise current distribution at turn-on operation, as depicted in Fig. 10 (b).

Fig. 12 illustrates the time variation of the noise current intensity. A sequence of the colored maps with 160 ns step represents the noise current generation and its propagation in the circuit. Fig. 12 (a) shows the intensity of time-synchronized 50 MHz near magnetic field at the turn-on operation. The dominant noise source is the hard recovery current of SiC SBD. It can be seen that the higher noise current level is distributed over a longer period for the type A configuration with fast turn on operation of Si IGBT than in case of the configuration of type B. Fig. 12 (b) depicts the intensity of time-synchronized 54 MHz near magnetic field at the turn-off operation. The slow-damped ringing oscillation current in turn-off operation of SiC MOSFET causes 20 dB or much higher than that of Si IGBT. This result qualitatively agree with the dynamic characteristics of transistor current shown in Fig. 5. Thus, the developed time-synchronized near magnetic field measurement can visualize the dynamic noise current behavior associating with the circuit operations. The

developed evaluation system can be applicable to identify noise source and to visualize noise propagation in existing power electronics circuits. It will be discussed continuously as a future work for designing the low-EMI power conversion circuit with WBG power devices based on the proposed noise visualization method.

V. Conclusion

This report discusses the dynamic behavior of noise current from Si and SiC power devices based on scanned time-synchronized near magnetic field measurement. The experimental results shown in this report demonstrate the usefulness of the developed time-synchronized near magnetic field scanning system to identify the EMI noise source and propagation of the power conversion circuit associated with switching operations. It will be useful to estimate the dynamic noise current distribution in the early stage of designing the power converter with next generation power devices with low-EMI characteristics.

Acknowledgment

This work was partially supported by JSPS Grants-in-Aid for Early-Career Scientists Grant Number 18K13744.

References

[1] A. M. Abou-Alfotouh, A. V. Radun, H.-R. Chang, and C. Winterhalter, "A 1-MHz hard-switched silicon carbide DC–DC converter," *IEEE Trans. Power Electron*., vol. 21, no. 4, pp. 880–889, Jul. 2006.

[2] Z. Zhang, F. Wang, L. M. Tolbert, B. J. Blalock, and D. J. Costinett, "Evaluation of switching performance of SiC devices in PWM inverter-fed induction motor drives," *IEEE Trans. Power Electron*., vol. 30, no. 10, pp. 5701–5711, Oct. 2015.

[3] D. Han and B. Sarlioglu, "Comprehensive study of the performance of SiC MOSFET-based automotive DC–DC converter under the influence of parasitic inductance," *IEEE Trans. Ind. Appl.*, vol. 52, no. 6, pp. 5100–5111, Nov./Dec. 2016.

[4] T. Kim, D. Feng, M. Jang, and V. G. Agelidis, "Common mode noise analysis for cascaded boost converter with silicon carbide devices," *IEEE Trans. Power Electron*., vol. 32, no. 3, pp. 1917–1926, Mar. 2017.

[5] Z. Fang, D. Jiang, Z. Shen, and R. Qu, "Impact of application of SiC devices in motor drive on EMI," *Proc. IEEE Appl. Power Electron. Conf. Expo. (APEC)*, pp. 652-658 Mar. 2017.

[6] T. Ibuchi and T. Funaki, "A comparative study on conducted noise characteristics of SiC and GaN power transistor," *Proc. 2016 International Symposium on Electromagnetic Compatibility (EMC EUROPE),* pp. 193-198, 2016.

[7] T. Ibuchi, E. Masuda, T. Funaki, H. Otake, T. Miyazaki, Y. Kanetake, Y. Sawai, and T. Nakamura, "Visualization of noise current distribution in an SiC power module using near-field magnetic scanning," *IEICE Comm. Exp.*, vol. 6, no. 10, pp. 584-589, 2017.

[8] J. B. Allen, "Short term spectral analysis, synthesis, and modification by discrete Fourier transform," *IEEE Trans. Acoust. Speech Signal Process.*, vol. 25, no. 3, pp. 235–238, 1977.